Many-body localization in a quantum simulator with programmable random disorder

J. Smith*, A. Lee*, P. Richerme†, B. Neyenhuis*, P. W. Hess*, P. Hauke‡§, M. Heyl‡§¶, D. A. Huse‖,

C. Monroe*

Generating the effective Hamiltonian We generate spin-spin interactions by applying spin-dependent

optical dipole forces to ions confined in a 3-layer linear Paul trap with a 4.8 MHz radial frequency.

Two off-resonant laser beams with a wavevector difference $\Delta\vec{k}$ along a principal axis of transverse

motion globally address the ions and drive stimulated Raman transitions. The two beams contain a

pair of beatnote frequencies symmetrically detuned from the resonant transition at $\nu_0 = 12.642819$

GHz by a frequency μ, comparable to the transverse motional mode frequencies. In the Lamb-

Dicke regime, this results in the Ising-type Hamiltonian in Eq. (1) [1–3] with

$$J_{i,j} = \Omega^2 \omega_R \sum_{m=1}^{N} \frac{b_{i,m} b_{j,m}}{\mu^2 - \omega_m^2}, \tag{2}$$

where Ω is the global Rabi frequency, $\omega_R = \hbar\Delta k^2/(2M)$ is the recoil frequency, $b_{i,m}$ is the normal-

mode matrix [4], and ω_m are the transverse mode frequencies. The coupling profile may be approx-

imated as a power-law decay $J_{i,j} \approx J_{max}/|i-j|^{\alpha}$, where in principle α can be tuned between 0

and 3 by varying the laser detuning μ or the trap frequencies ω_m [2,5]. In this work, α was tuned ap-

*Joint Quantum Institute, University of Maryland Department of Physics and National Institute of Standards and Technology, College Park, MD 20742

†Department of Physics, Indiana University, Bloomington, IN, 47405

‡Institute for Quantum Optics and Quantum Information of the Austrian Academy of Sciences, 6020 Innsbruck, Austria

§Institute for Theoretical Physics, University of Innsbruck, 6020 Innsbruck, Austria

¶Physik Department, Technische Universitt Mnchen, 85747 Garching, Germany

‖Physics Department, Princeton University, Princeton, NJ 08544, USA

16   proximately between 0.95 and 1.81 by changing μ. By asymmetrically adjusting the laser beatnote

17   detuning μ about the carrier by a value of B we apply a global Stark shift that can be thought of as

18   a uniform effective transverse magnetic field of $(B/2)\sigma_i^z$.

19   We generate the effective disorder by applying a site-dependent Stark shift using a single

20   355nm laser beam that is focused down tightly to a $1/e^2$ waist of $\sim 1.8\mu m$. The ion separation is

21    $\sim 2.5\mu m$, thus the crosstalk between ions is negligible with a measured ratio of nearest-neighbor

22   Rabi frequencies of $\sim 20 : 1$. We use an acousto optic modulator (AOM) with a full width at half

23   maximum bandwidth of $\approx$100 MHz to apply the Stark shift to each ion. The AOM is not imaged

24   onto the ions, so that driving the AOM with different frequencies allows the position of the beam to

25   be scanned over the length of a 10 ion chain, $\sim 20\mu m$. The Stark shift is proportional to I^2. Thus,

26   to achieve larger applied Stark shifts, we raster through the AOM drive frequencies corresponding

27   to addressing each ion with a total cycle time of $\sim 5\mu s$ instead of applying them simultaneously.

28   Since we cannot control the sign of the site-specific Stark shift, to center the disorder strength

29   around the global transverse field, we adjust the asymmetric detuning by $W J_{max}/2$.

30   **Sampling Error** We determine that averaging over 30 different random realizations of disorder is

31   sufficient to have a sampling error smaller than the effect we observe by looking at the change in

32   the time-averaged HD with respect to a change in the disorder strength. Figure 3b makes explicit

33   that this error is much smaller than than the change in the time-averaged HD with respect to a

34   change in the disorder strength.

35   **Measuring the spin-spin coupling matrix** In order to observe the dynamics between just two

36   of the ions in the chain, we shelve the other spins out of the interaction space. This is done

37   by performing a π rotation between $|\downarrow\rangle_z$, $^2\mathrm{S}_{1/2}\,|F = 0, m_F = 0\rangle$, and one of the Zeeman states,

38   $^2\mathrm{S}_{1/2}\,|F = 1, m_F = -1\rangle$, while shifting the two ions of interest out of resonance by applying a

39   large Stark shift with the individual addressing beam. We then apply our Hamiltonian which now

40   acts only on the two ions left in the interaction space and determine the elements of the spin-spin

41   coupling matrix by fitting the measured interaction Rabi flopping frequency between each pair of

42   spins.

43   **Arbitrary product state preparation** State initialization starts with optically pumping the spins

44   with high-fidelity to $|\downarrow\downarrow\downarrow \cdots\rangle_z$. Then we perform a global $\pi/2$ rotation to bring the ions to

45   $|\downarrow\downarrow\downarrow \cdots\rangle_x$. At this point we apply a Stark shift with the individual addressing beam to the spins

46   that are to be flipped and allow the chain to evolve until these ions are π out of phase with rest

47   of the ions. This, along with our ability to perform high fidelity global rotations, allows for the

48   preparation of any arbitrary product state along any direction of the Bloch sphere. Individual spin

49   flips can be achieved with a fidelity of ~ 0.97, while arbitrary state preparation can be done with a

50   fidelity of $\sim (0.97)^N$, where N is the number of spins flipped with the individual addressing beam.

51   **Determining a Set of Thermalizing Parameters** Extended Data Figure 1 shows the time evolu-

52   tion of $\langle\sigma_i^x\rangle$ for different values of B for the spins initialized in the randomly chosen product state

53   $|\downarrow\downarrow\downarrow\uparrow\downarrow\downarrow\downarrow\uparrow\downarrow\uparrow\rangle_x$. Without a transverse field, the spins are in an eigenstate of the Ising interaction

54   and undergo no evolution. Once a transverse field is added the individual spins begin to lose mem-

55 ory of their initial conditions and as its strength is increased, the ions thermalize faster and more

56 robustly.

57   To confirm the system is thermalizing, we measure the time evolution of the single site mag-

58 netization, $\langle \sigma_i^z \rangle$, along an orthogonal direction for different strengths of the transverse magnetic

59 field starting with the spins initialized in the Néel ordered state. As seen in Extended Data Fig. 1

60 the spins have lost information about their initial conditions in the z direction for all values of B.

61   We calculate the spectral statistics of adjacent energy levels for the Hamiltonian and find they

62 are not Poisson distributed for $B = 4J_{max}$ and $D_i = 0$ indicating that with no applied disorder, the

63 system is not in a localized phase. Furthermore, one can determine if a system is in a thermal or

64 localized regime by finding the correlation between adjacent energy splittings by calculating the

65 ratio of two consecutive gaps[6]:

$$r_n = \frac{min\{\delta_n, \delta_{n-1}\}}{max\{\delta_n, \delta_{n-1}\}} \tag{3}$$

66 where $\delta_n = E_{n+1} - E_n \geq 0$. For a localized phase, where one expects a Poisson energy spectrum,

67 the probability distribution of this order parameter is given by $P_p(r) = 2/(1 + r)^2$ and thus $\langle r \rangle \approx$

68 0.39. For energy level spacings following a random-matrix as predicted for a thermalizing regime,

69 we calculate $\langle r \rangle \approx 0.53$ for a chain of 10 spins. Extended Data Figure 2 shows that $\langle r \rangle$ saturates

70 to the expected value for a random matrix distribution, indicating that the Hamiltonian is thermal

71 for sufficiently large B.

72   **Calculating the density matrix expected by the Eigenstate Thermalization Hypothesis**   Given

73   a Hamiltonian and an initial state $|\psi_0\rangle$, the corresponding energy is $\langle\psi_0|\,H\,|\psi_0\rangle$. For a thermalizing

74   system satisfying ETH this energy should be equal to the classical energy:

$$E = \frac{\mathrm{Tr}[He^{-\beta H}]}{\mathrm{Tr}[e^{-\beta H}]} \tag{4}$$

75   for the appropriate $\beta = 1/(k_B T)$. When partitioning the entire system into subsystems A and B,

76   with the size of A much smaller than B (perhaps even a single spin), then, the density matrix on

77   site A at long times can be approximated by:

$$\rho_A = \frac{\mathrm{Tr_B}[e^{-\beta H}]}{\mathrm{Tr}[e^{-\beta H}]} \tag{5}$$

78   Since we start in the Néel ordered state, the initial energy given the Hamiltonian in Eq. (1)

79   is equal to zero, $\langle\psi_0|\,H\,|\psi_0\rangle = 0$. Equating this to the right hand side of Eq. (4) and solving for

80   β gives $\beta = 0$, or $T = \infty$. Using this β in Eq. (5) gives a value for any reduced thermal density

81   matrix of:

$$\begin{pmatrix} 1/2 & 0 \\ 0 & 1/2 \end{pmatrix}$$

82   in agreement with the measured reduced density matrices in Fig. 2a.

83   **Comparison to Numerics**   To demonstrate the MBL we observe is a general feature of our Hamil-

84   tonian we perform numerical simulations using exact diagonalization. Extended Data Figure 3

85   compares the experimentally measured time evolution of the normalized HD with numerics and

86   shows excellent agreement between them. We see similar agreement between experimental data

87   and numerics for the time evolution of the single-spin magnetizations (not shown). The aspects of

88   MBL we experimentally measure were independently verified numerically as generic characteris-

89   tics of $(1)^{7}$.

90   **Decoherence and Dephasing** To measure our system's coupling to the environment we fit an

91   exponential decay to the dynamics in the upper left panel of Extended Data Fig. 1 as we expect

92   no time evolution of $\langle \sigma_i^x \rangle$ because the initial state is an eigenstate of the Hamiltonian and thus any

93   dynamics give an estimate of the decoherence rate. We find this estimate to be $J_{Max}t = 64.6$ which

94   is approximately 60 times slower than the dynamics of the localization.

95   Extended Data Fig. 4 shows a numerical simulation of the extended dynamics for the model

96   Hamiltonian with (green curves) and without (blue curves) crosstalk error between ions from the

97   individual addressing and laser intensity noise on the Ising couplings. It is clear that the localization

98   persists well beyond the experimental timescales even when accounting for experimental noise.

99   We model the crosstalk noise on the disordered field by adding 5% of the Stark shift applied

100   to adjacent ions to the size of the intended Stark shift which is consistent with the spillover we

101   measure between ions. To incorporate noise on the spin-spin couplings, we scale the strength of

102   the Ising couplings by a value we pull randomly from a Gaussian distribution centered around

103    $\mu = 1$ with $\sigma = 0.05$ for each instance of disorder because the laser intensity noise is slower

104   than the duration of an experiment. The size of this simulated noise is consistent with the directly

105   measured noise on $J_{i,j}$.

106   **Quantum Fisher Information** The quantum Fisher information (QFI) has recently been shown

107   to witness genuinely multipartite entanglement [8,9]. From a quantum metrology perspective, the

108 QFI quantifies the sensitivity of a given input state to a unitary transformation $e^{i\vartheta\hat{\mathcal{O}}}$ generated by

109 the hermitian operator $\hat{\mathcal{O}}$. In a pure state, it is given by [10]

$$F_Q = 4(\Delta\hat{\mathcal{O}})^2 = 4(\langle\hat{\mathcal{O}}^2\rangle - \langle\hat{\mathcal{O}}\rangle^2). \tag{6}$$

110 For a local operator $\hat{\mathcal{O}} = \sum_{i=1}^{N}\hat{\mathcal{O}}_i$ (where the difference between largest and smallest eigen-

111 value of $\hat{\mathcal{O}}_i$ is 1), the QFI witnesses entanglement as soon as

$$f_Q \equiv F_Q/N > 1\,. \tag{7}$$

112 To characterize the growth of entanglement out of the initial Néel state, the natural choice

113 of the generator $\hat{\mathcal{O}}$ is the staggered magnetization, $\hat{\mathcal{O}} = \sum_{i=1}^{N}(-1)^i\sigma_i^z/2$. Remarkably, this QFI is

114 proportional to the variance of the HD $\mathcal{D}(t)$ given by Eq. (2) of the main text,

$$F_Q = 4N^2(\Delta\hat{\mathcal{D}})^2 = \sum_{i,j}[(-1)^{i+j}\langle\sigma_i^z\sigma_j^z\rangle] - [\sum_i(-1)^i\langle\sigma_i^z\rangle]^2, \tag{8}$$

115 when associating $\mathcal{D}(t) = \langle\hat{\mathcal{D}}(t)\rangle$, with $\hat{\mathcal{D}} = 1/(2N)[1 - \sum_{i=1}^{N}(-1)^i\sigma_i^z]$.

116 The QFI as defined in Eq. (6) assumes a pure state, i.e., that time evolution is purely unitary.

117 For mixed states, the QFI cannot be expressed as a simple expectation value of the operator $\hat{\mathcal{O}}$[10].

118 In general, decoherence reduces the purity of the system's state over experimental time scales. To

119 show that the measured increase of F_Q as defined in Eq. (8) is indeed due to coherent dynamics, we

120 compare to numerical calculations for a unitary time evolution using the experimental parameters.

121 Extended Data Fig. 5 shows the experimental data is always below the theoretical prediction for

122 a unitary time evolution. The loss of purity or other experimental imperfections such as detection

123 error, therefore, do not generate a false positive indicator of entanglement in our system.

124   Extended Data Figure 6 further establishes this point, showing an increase in the QFI we

125 measure and strong agreement between experimental data and theory when postselecting for mea-

126 sured states with 5-spin excitations. We postselect because when $B \gg J$ the Hamiltonian is

127 effectively an XY model and conserves $\sum_i \sigma_i^z$, because Ising processes that flip spins along the

128 large field are energetically forbidden. However, because of camera detection error we find there is

129 significant leakage out of states with 5-spin excitations ($\approx 70\%$ expected numerically, $\approx 35\%$ de-

130 tected) into states with 4 and 6-spin excitations ($\approx 20\%$ detected) which should not be populated

131 as the transverse magnetization is conserved modulo two spin flips in the transverse field Ising

132 model. Thus, we post-select for states with 5-spin excitations. Extended Data Figures 5 and 6

133 show a clear difference between the interacting case and a theory of free-fermions (see below) for

134 the experimental data and numerical simulations, thus, establishing that the growth in QFI in the

135 data and full-Hamiltonian numerics are due to a many-body effect.

136   To study how the localization changes with system size, we performed a numerical finite-size

137 scaling. In order to obtain a well-behaved scaling, we use the Kac prescription[11], i.e., we adjust

138 the couplings as $J_{ij} = J\mathcal{N}^{-1}|i-j|^{-\alpha}$, where $\mathcal{N} = (N-1)^{-1}\sum_{i<j}|i-j|^{-\alpha}$. Note that using

139 this prescription the fundamental energy scale J differs by about a factor of 2 from J_{max}, the value

140 used in the main text.

141   For $\alpha > 2$, the disordered long-range Ising Hamiltonian shows MBL behavior at large

142   disorder[12]. In Extended Data Fig. 7, we plot the dynamics of the QFI for $\alpha = 3$, where it grows

143   consistent with the characteristic long-time growth of entanglement for an MBL state. In par-

144   ticular, within a time window $2^\alpha < tJ < 3^\alpha$ where only next-nearest-neighbor interactions are

145   relevant, the system essentially behaves as a nearest-neighbor Ising model with a weak next-to-

146   nearest-neighbor coupling. For such a system, a logarithmic growth of entanglement is expected,

147   as we indeed find in that regime, see inset in Extended Data Fig. 7.

148   Moreover, in Extended Data Fig. 7, we compare our numerical results to the appropriate

149   long-range free-fermionic theory (see below), which shows a quick system-size independent sat-

150   uration of the QFI without further growth. Therefore, we conclude that the observed increase of

151   the QFI is not possible in a quantum system without many-body interactions, thus giving a clear

152   signature for true MBL behavior.

153   The situation is more complex at $\alpha = 1.13$. For $B = 0$, it has been predicted that within

154   the range $1 < \alpha < 2$ delocalized behavior could be expected in the thermodynamic limit[12]. As

155   seen in Extended Data Fig. 8, for the considered system sizes up to $N = 14$ the model displays all

156   essential signatures of MBL, as found for $\alpha = 3$. However, the important question of whether this

157   localization persists in the thermodynamic limit can only be addressed with system sizes larger

158   than those accessible using exact diagonalization. Here, scaling our quantum simulator to larger

159   system sizes could thus resolve a difficult open question, namely of the existence of ergodicity in

160   the range $1 < \alpha < 2$. However, we would like to emphasize that the essential features of MBL

161   are nevertheless captured by the 10-spin experimental system. In particular, we still find a time

162 window consistent with a logarithmic growth of entanglement, see inset in Extended Data Fig. 8.

163 In order to make a stronger connection between growth in the QFI and growth of entangle-

164 ment we calculate the entropy of entanglement between two halves of the chain:

$$S_A = -Tr[\rho_A \log \rho_A] \tag{9}$$

165 where $\rho_A = Tr_B[\rho]$ and B is the other half of the spin chain. The entanglement entropy quantifies

166 the number of entangled bits between two subsystems.

167 In Extended Data Figs. 7 and 8 it is clear that there is long-time growth of the entanglement

168 entropy that is consistent with the expected growth for a MBL state[13,14] and is absent in the free-

169 fermion numerics. The difference between the numerics for the model Hamiltonian and the non-

170 interacting theory for the QFI and the entanglement entropy in Extended Data Figs. 9 and 10

171 distinguishes between the two cases for the experimental system size and timescale. These figures

172 also establish a qualitative connection between growth in the QFI and growth in entanglement.

173 To show that the QFI growth is truly due to interactions, we also compare numerics with the

174 experimentally applied Hamiltonian to a close approximation of H, Eq. (1) of the main text, with a

175 non-interacting theory. Using the Jordan-Wigner transformation, $\sigma_j^- \to e^{-i\theta_j} c_j$, with the phase of

176 the string operator $\theta_j = \pi \sum_{j<i} c_j^\dagger c_j$, the Hamiltonian Eq. (1) can be mapped to a fermionic theory

177 with annihilation and creation operators c_j and $c_j^\dagger$, respectively,

$$H = \sum_{i<j} J_{ij}(c_i^\dagger e^{i(\theta_j - \theta_i)} c_j + c_i^\dagger e^{i(\theta_j + \theta_i)} c_j^\dagger + h.c.) - \sum_i (B + D_i) c_i^\dagger c_i . \tag{10}$$

178 If J_{ij} contained only nearest-neighbor interactions, this Hamiltonian would become equivalent

10

to a free-fermionic theory. For general J_{ij}, however, the string operators generate interactions between the fermions. Over short times, and especially in a localized regime, the phases θ_j are dominated by their initial values, i.e., it is a good approximation to replace (for the initial Neel state) $\theta_j \to \pi \sum_{j<i} ((-1)^j + 1)/2$ in the Hamiltonian. This replacement amounts to approximating H by a non-interacting fermionic theory with long-range hopping and pairing. The QFI for that case is included in Extended Data Figs. 7 and 8. As one can see, the QFI quickly saturates to values below $f_Q = 1$. The experimentally and numerically observed further growth of the QFI is thus truly due to interactions, and cannot be captured within a free-fermionic theory, even with long-range hopping.

1. Mølmer, K. & Sørensen, A. Multiparticle Entanglement of Hot Trapped Ions. *Phys. Rev. Lett.* **82**, 1835-1838 (1999).

2. Porras, D. & Cirac, J. I. Effective Quantum Spin Systems with Trapped Ions. *Phys. Rev. Lett.* **92**, 207901 (2004).

3. Kim, K. *et al.* Entanglement and Tunable Spin-Spin Couplings between Trapped Ions Using Multiple Transverse Modes. *Phys. Rev. Lett.* **103**, 120502 (2009).

4. James, D. F. V. Quantum dynamics of cold trapped ions with application to quantum computation. *Applied Physics B* **66**, 181-190 (1998).

5. Islam, R. *et al.* Emergence and Frustration of Magnetism and Variable-Range Interactions in a Quantum Simulator. *Science* **340**, 583-587 (2013).

11

199   6. Oganesyan, V. & Huse, D. A. Localization of interacting fermions at high temperature. *Phys.*

200   *Rev. B* **75**, 155111 (2007).

201   7. Wu, Y-L. & Das Sarma, S. Understanding analog quantum simulation dynamics in coupled

202   ion-trap qubits. *Phys. Rev. A* **93**, 022332 (2016).

203   8. Hyllus, P. *et al.* Fisher information and multiparticle entanglement. *Phys. Rev. A* **85**, 022321

204   (2012).

205   9. Tóth, G. Multipartite entanglement and high precision metrology. *Phys. Rev. A* **85**, 022322

206   (2012).

207   10. Braunstein, S. L. & Caves, C. M. Statistical distance and the geometry of quantum states.

208   *Phys. Rev. Lett.* **72**, 3439-3443 (1994).

209   11. Kac, M. Can One Hear the Shape of a Drum? *Am. Math. Monthly* **73**, 1-23 (1966).

210   12. Burin, A. L. Energy delocalization in strongly disordered systems induced by the long-range

211   many-body interaction. *arXiv:cond-mat/0611387* (2006).

212   13. Bardarson, J. H., Pollmann, F. & Moore, J. E. Unbounded Growth of Entanglement in Models

213   of Many-Body Localization. *Phys. Rev. Lett.* **109**, 017202 (2012).

214   14. Pino, M. Entanglement growth in many-body localized systems with long-range interactions.

215   *Phys. Rev. B* **90**, 174204 (2014).
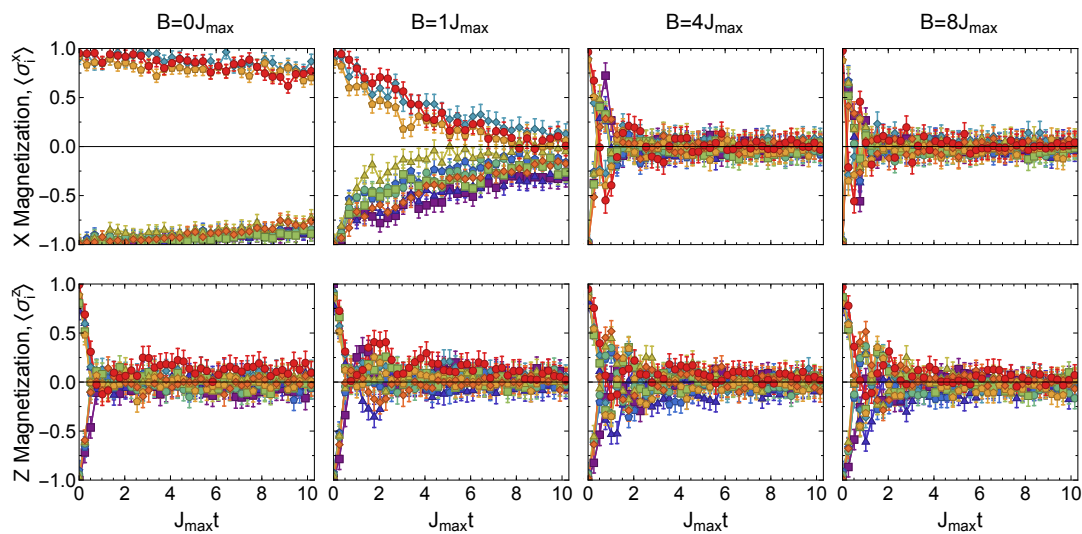
Extended Data Figure 1: **Measured thermalization in the transverse field Ising model.** The upper panels show the time dynamics of $\langle \sigma_i^x \rangle$ (different colors represent different ions) for 10 spins prepared in the random product state $|\downarrow\downarrow\downarrow\uparrow\downarrow\downarrow\downarrow\uparrow\downarrow\uparrow\rangle_x$, for different transverse magnetic field strengths. For $B = 0$ the spins are in a eigenstate and do not thermalize. However, as the strength of B is increased the system begins to thermalize more robustly and quickly. The lower panel plots the time evolution of $\langle \sigma_i^z \rangle$ with 10 spins prepared in the Néel ordered in the z direction for different transverse magnetic field strengths. We conclude that the system is in the thermalizing regime for $B = 4J_{max}$ since we observe thermalizing behavior along two orthogonal directions. Error bars are 1 standard deviation of statistical error.
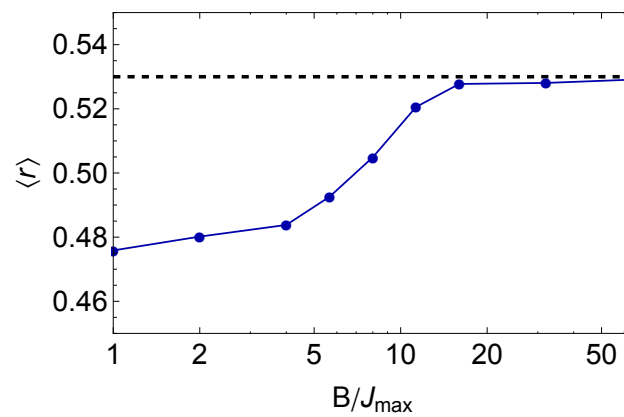
226

227 Extended Data Figure 2: **Thermalizing level statistics.** The calculated value of $\langle r \rangle$ with respect

228 to B saturates close to the predicted value for a random-matrix distribution (dashed black line)

229 implying that the Hamiltonian is in the thermal phase for sufficiently large B.

14
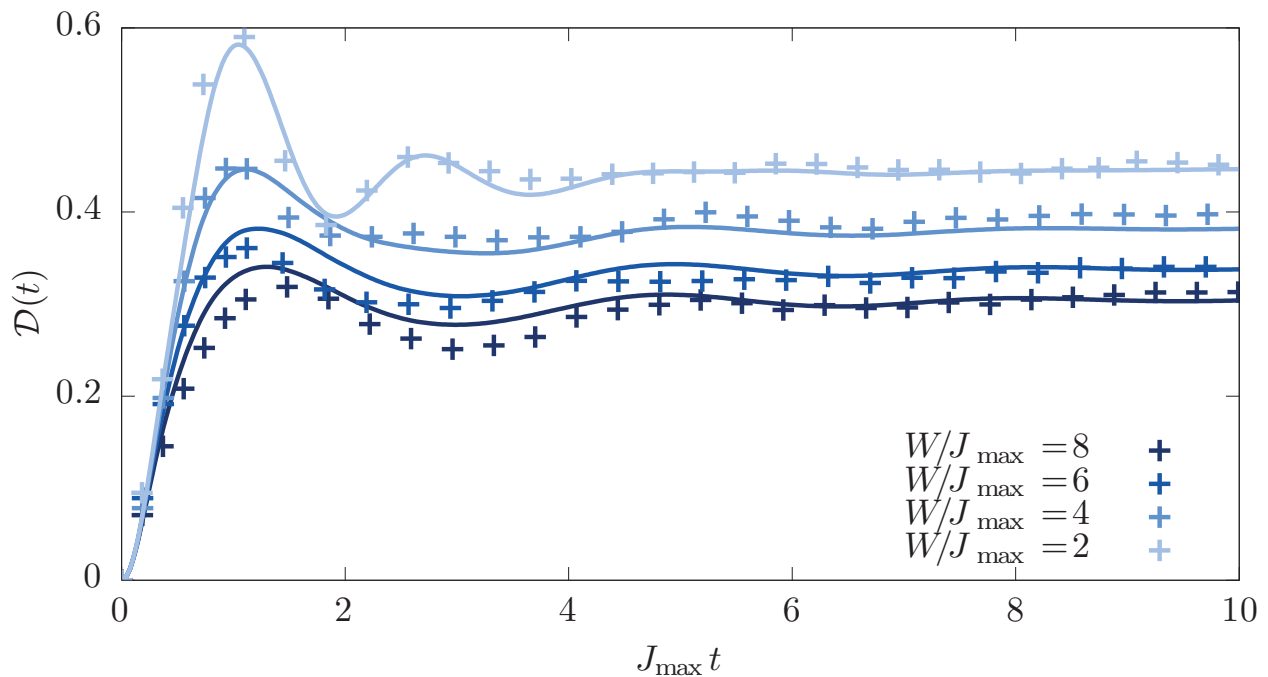
Extended Data Figure 3: **Comparison of the experimental data (crosses) with exact numerical simulations (blue lines) for normalized Hamming distance.** There is excellent agreement between the numerical simulations using the experimental parameters and the measured data. This demonstrates that the observed effects are general features of the Hamiltonian.

15
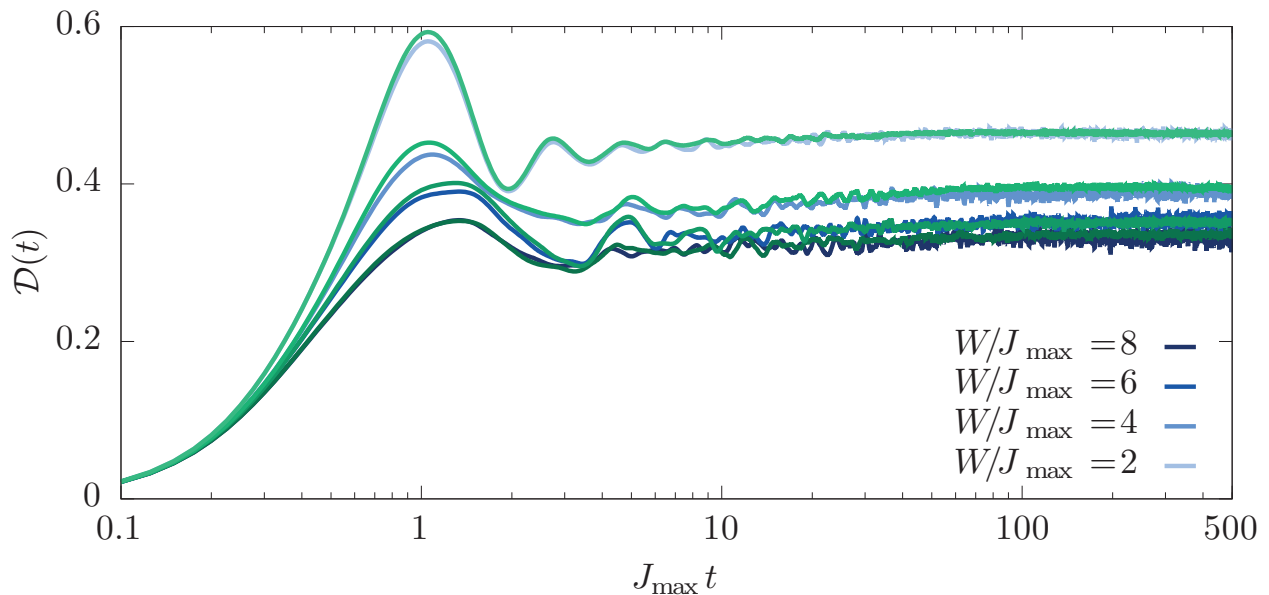
Extended Data Figure 4: **Numerical simulations of the extended time evolution of the Hamming distance for the model Hamiltonian (blue curves) and with experimental noise (green curves).** The localization we observe persists much longer than the experimental timescale in the model Hamiltonian (blue curves) even when accounting for laser intensity noise and crosstalk between the ions from the individual addressing beam (green curves).
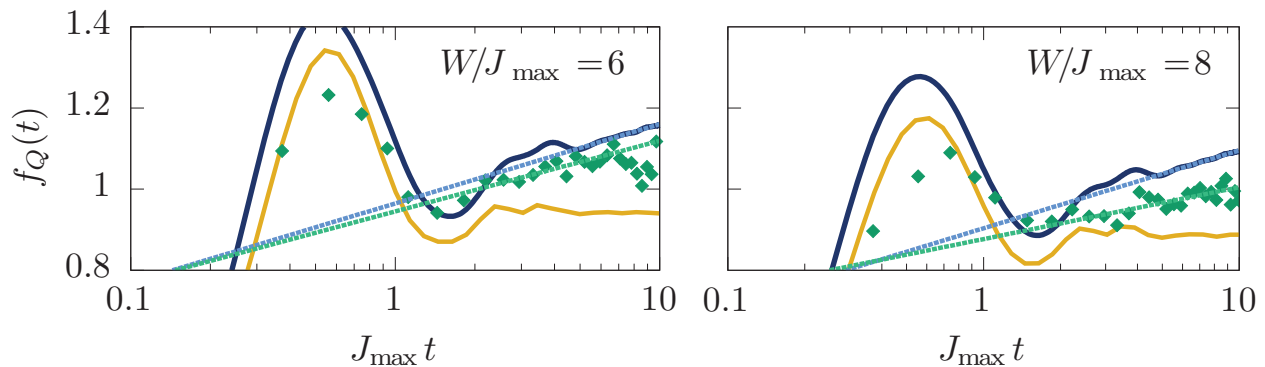
Extended Data Figure 5: **Comparison of experimental data (green dots) with exact numerical simulations for the experimentally applied Hamiltonian (thick blue lines) and free-fermion Theory (orange) for QFI.** The solid straight lines represent logarithmic fits to the numerical (light blue) and experimental data (light green). Deviations from the ideal coherent dynamics due to decoherence and other imperfections in the experimental setup, such as detection error, lead to a reduction of the QFI. Importantly, this suggests that experimental imperfections do not generate a false positive for entanglement. Moreover, there is long-time growth in the QFI from the measured data and applied Hamiltonian numerics that is absent in the free-fermion theory.
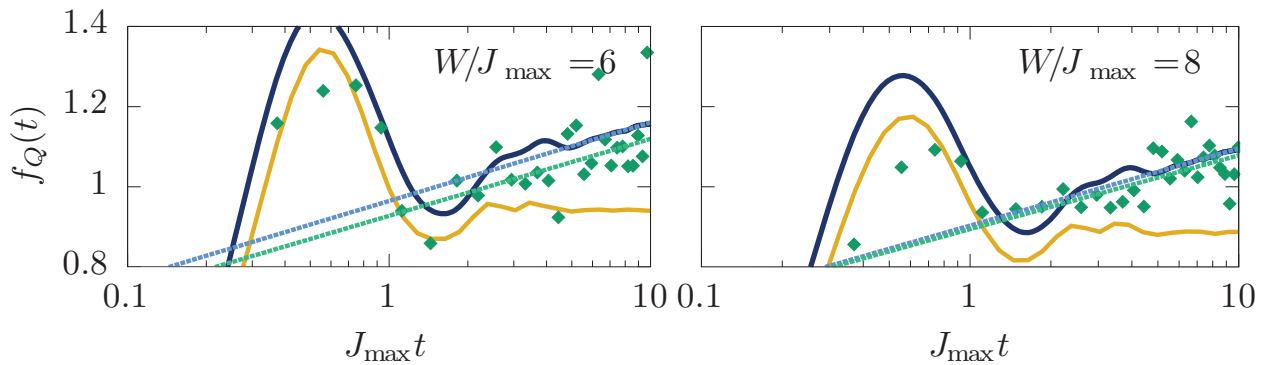
Extended Data Figure 6: **Comparison of postselected experimental data (green dots) with exact numerical simulations for the experimentally applied Hamiltonian (thick blue lines) and free-fermion Theory (orange) for QFI.** The solid straight lines represent logarithmic fits to the numerical results for the experimentally applied Hamiltonian (light blue) and postselected data for results with 5 spin flips (light green). The increase in the postselected QFI and the agreement between the postselected data and numerical simulations supports the claim that experimental imperfections decrease the value of the QFI for the full experimental data.
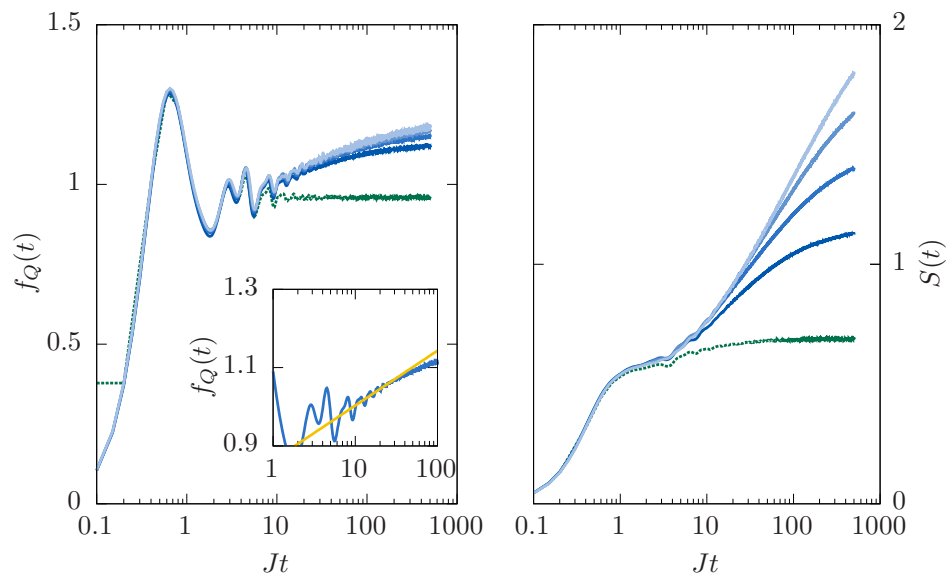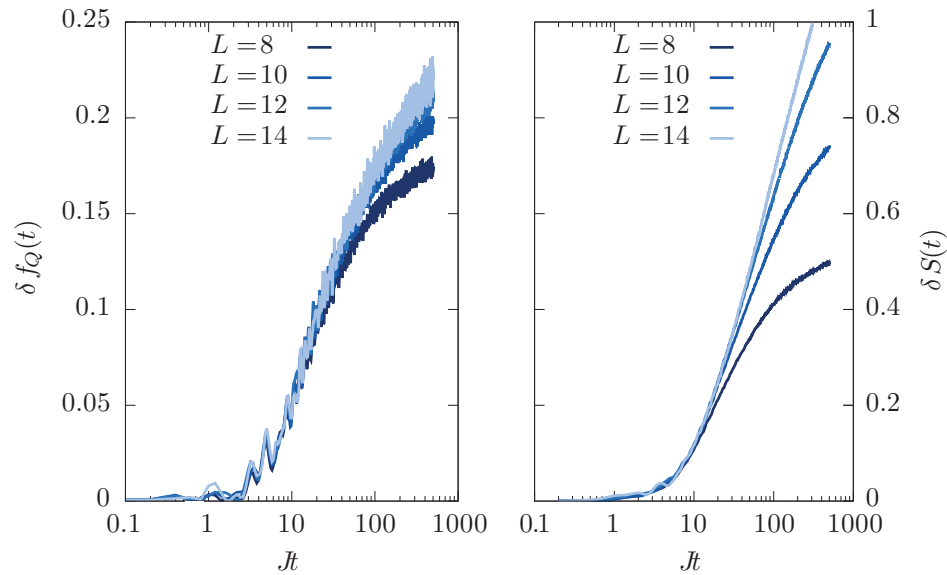
Extended Data Figure 7: **QFI and entanglement entropy from exact diagonalization ($\alpha = 3$ and $W/J = 8$).** Left panel: When subject to disorder, the QFI of the staggered magnetization shows a characteristic growth of entanglement (blue lines; from dark to light: $N = 8, 10, 12, 14$ averaged over $10^6, 3 \times 10^5, \ldots, 2500$ disorder realizations). This growth is absent in a theory of free-fermions with long-range hopping and pairing (green dashed lines with $N = 14$ (dark green) averaged over 10000 realizations). Left panel inset: In a time window dominated by next-nearest neighbor interactions, $2^\alpha < tJ < 3^\alpha$, one observes a characteristic logarithmic entanglement growth, expected for a MBL system with short-range interactions. Right panel: The entanglement entropy between two halves of the chain shows long-time logarithmic growth for the interacting case and saturates for the free-fermion theory consistent with the expectation for a MBL state and single-particle localized state, respectively, and a qualitative agreement between growth in QFI and entanglement entropy.
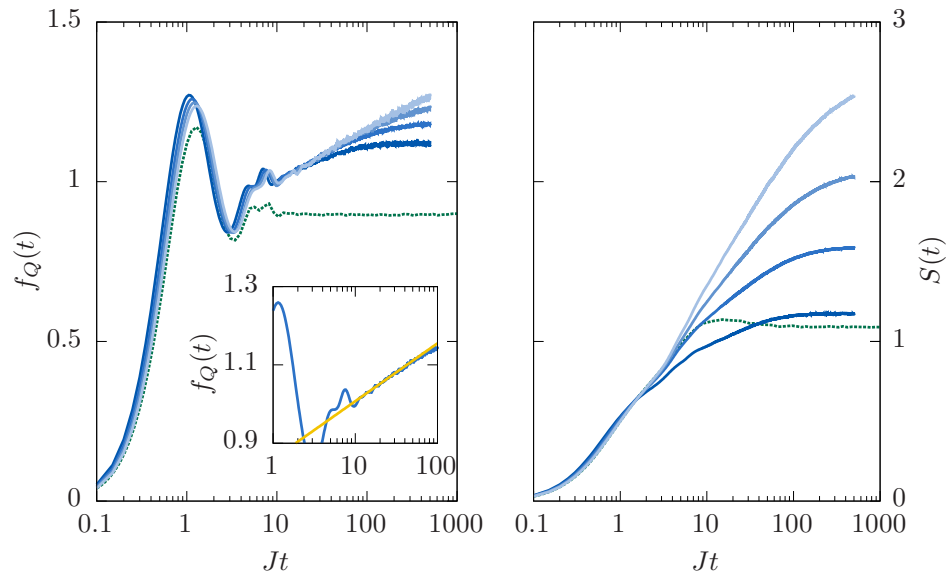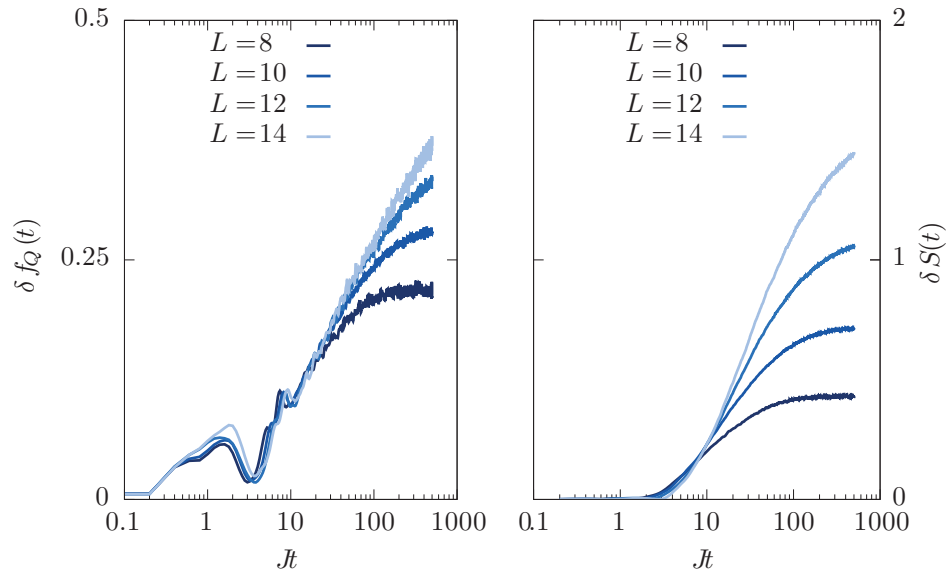
Extended Data Figure 8: **QFI and entanglement entropy from exact diagonalization ($\alpha = 1.13$ and $W/J = 8$).** Same color coding as in Extended Data Fig. 7. Importantly, for the experimentally relevant system size of N = 10, we again find a time window consistent with a logarithmic growth of entanglement in the growth of QFI (see left inset) and half-chain entanglement entropy.

Extended Data Figure 9: **Difference between numerics for the interacting model Hamiltonian and free-fermion theory for QFI and entanglement entropy ($\alpha = 3$ and $W/J = 8$).** There is a clear departure between the numerically calculated QFI and entanglement entropy for the model Hamiltonian and the free-fermion theory.

Extended Data Figure 10: **Difference between numerics for the interacting model Hamiltonian and free-fermion theory for QFI and entanglement entropy ($\alpha = 1.13$ and $W/J = 8$).** There is a clear departure between the numerically calculated QFI and entanglement entropy for the model Hamiltonian and the free-fermion theory for N=10 on the experimental timescale.